Journal Pre-proof

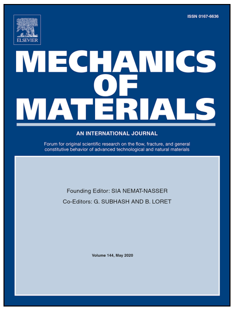

Tuning structural and mechanical anisotropy of PVA hydrogels

Sidi Duan, Zixiao Liu, Shuwang Wu, Mutian Hua, Ximin He

PII: S0167-6636(22)00181-8

DOI: https://doi.org/10.1016/j.mechmat.2022.104411

Reference: MECMAT 104411

To appear in: *Mechanics of Materials*

Received Date: 14 March 2022

Revised Date: 30 June 2022

Accepted Date: 12 July 2022

Please cite this article as: Duan, S., Liu, Z., Wu, S., Hua, M., He, X., Tuning structural and mechanical anisotropy of PVA hydrogels, *Mechanics of Materials* (2022), doi: https://doi.org/10.1016/j.mechmat.2022.104411.

Tuning structural and mechanical anisotropy of PVA Hydrogels

Sidi Duan[#a], Zixiao Liu[#a], Shuwang Wu[a,b], Mutian Hua[a], Ximin He[a,*]

[a] Department of Materials Science and Engineering, University of California Los Angeles, Los Angeles, CA 90095, USA
[b] State Key Laboratory of Radiation Medicine and Protection, School for Radiological and Interdisciplinary Sciences (RAD-X), Soochow University, Suzhou, Jiangsu 215123, China
[#] These authors contributed equally
[*] Corresponding author. E-mail address: ximinhe@ucla.edu

Abstract

Hydrogel materials are widely applicable due to their high water content, biocompatibility, and broad tunability. While the overall mechanical performance of hydrogels can be tuned by methods such as altering the recipe, introducing a secondary network, and adding a post-treatment step, anisotropic mechanical properties with specific anisotropic ratios are not readily achievable. Moreover, the relation between anisotropic structures and the resulting difference in mechanical performance along various directions is not yet clearly understood. In this paper, we fabricated poly(vinyl alcohol) hydrogels with tunable anisotropic ratios of Young's moduli by a bidirectional ice-templating method. Then we characterized the morphologies and mechanical properties in different directions to study the correlation between structure and property anisotropy. An analytical model based on Eshelby's equivalence principle and Mori-Tanaka's mean-field theory was established to predict the theoretical values of the anisotropic effective moduli for the porous hydrogels, which agrees well with the experimental results. This model reveals the key parameter that describes the extent of anisotropy and has the potential of providing guidance for designing micro-structured hydrogels with specified mechanical properties.

Keywords

Anisotropic hydrogel, tunable mechanical properties, micromechanics, microporous structure

1. Introduction

Hydrogels are three-dimensional (3D) polymer networks that swell in water. Due to their similarity to biological tissues with highly porous structures and high water content, hydrogel materials find a wide range of applications in biomedical engineering (Chai et al., 2017), soft robotics (Lee et al., 2020; Zhao et al., 2021), soft sensors (Tang et al., 2020), wearable electronics (Xiao et al., 2021; Yao et al., 2022), etc. The broad choices of polymers and cross-linking methods, variable constituents of precursor solutions, and diverse post-treatments endow hydrogels with enormous space for tuning their structures and properties (Wang et al., 2020). Researchers have developed a variety of methods to control the mechanical properties of hydrogels. For example, altering the type, size, and concentration of crosslinkers can effectively change the elastic moduli of hydrogels (Eiselt et al., 1999). Using ions or co-solvents can tune the porous structures, modulus, and strength of hydrogels by modulating the polymer chain aggregation (Alsaid et al., 2021; Hua et al., 2021; Khodambashi et al., 2021; Sadeghi and Jahani, 2012; Wu et al., 2021). Introducing a second polymer network to form double-network hydrogels results in toughening, due to the local yielding mechanism (Gong, 2010; Li et al., 2015; Sun et al., 2012). The effects of these methods on the microstructures of hydrogels are isotropic, which means that mechanical performances in all directions change simultaneously.

However, there are cases where it requires anisotropic materials with specific anisotropy ratios, which refers to the ratio between moduli in different directions of the material. For instance, various biomedical implants are required to match the anisotropic mechanical properties of tissues. Biological soft tissues grown in the human body often adopt anisotropic structures with different moduli in parallel ($E_{\parallel}$) and perpendicular directions ($E_{\perp}$) (Roger C. Haut, 2002). Examples include human myocardium ($E_{\parallel}$=0.1GPa, $E_{\perp}$=0.03GPa) (Hoffmeister et al., 1996), human coronary arteries intimal strips ($E_{\parallel}$=600kPa, $E_{\perp}$=180kPa), media strips ($E_{\parallel}$=40kPa, $E_{\perp}$=7kPa), and adventitia strips ($E_{\parallel}$=180kPa, $E_{\perp}$=90kPa) (Holzapfel et al., 2005). Mechanical property matching between the implant and the tissue is crucial to the function of the implant since an implant softer than the native tissue will not be strong enough to provide support, while a stiffer implant will cause foreign body reactions (Carnicer-Lombarte et al., 2019). Thus, implants need to have not only comparable stiffness but also similar anisotropy ratios to these tissues. Apart from tissue-mimicking biomedical implants, anisotropically structured hydrogels are also desired for drug delivery when distinct diffusion rates are required for different directions (Wu et al., 2012), as well as for cell culturing where cell adhesion and differentiation are influenced by directionally distinct scaffold morphology (McClendon and Stupp, 2012).

Anisotropic hydrogels can be fabricated via a variety of methods. Electrospinning can produce hydrogels with anisotropic ratios ranging from 1 to 1.5 by changing the mandrel velocity (Courtney et al., 2006), but it is not suitable for large volume fabrication (Nune et al., 2017). Other methods utilize 3D printing to produce anisotropic hydrogels by directly printing aligned structures (Boley et al., 2019), multi-material printing (Goh et al., 2018), or applying external forces (Kim et al., 2018). The anisotropy ratios of hydrogels fabricated by 3D printing can take the value from 1 to over 10. These methods are limited by the choice of materials, the difficulty of printing specific structures, and the defects caused by layer-by-layer printing (Chen et al., 2021). Moreover, physically crosslinking the hydrogel by ions while stretching can also produce anisotropic mechanical properties (Ma et al., 2020). The limitation of this method is that the anisotropy cannot be retained without the presence of specific ions, which is the case in most biological applications. Ice templating is also a common method for fabricating anisotropic structures. Unidirectional freezing of aqueous hydrogel precursor induces ice crystal growth in the direction of temperature gradient and results in aligned porous structures (Nelson and Naleway, 2019; Zhao et al., 2020), however, it cannot control the anisotropy ratio, since the features in the plane perpendicular to the freezing direction either are isotropic or adopt random orientations. Researchers have shown that the addition of a second temperature gradient perpendicular to the first temperature gradient can effectively align the anisotropic structures, namely lamellar structures, in that direction (Bai et al., 2015; Min et al., 2021). Moreover, if ice templating of the hydrogel precursor results in lamellar structures, then the states between randomly orientated lamellar structure and completely aligned lamellar structure will possess different anisotropy ratios. Although various anisotropy ratios can be achieved via bidirectional ice templating, the alignment of the structures has not been well characterized, and the relation between the alignment and the anisotropy ratio has yet to be analyzed to gain a better understanding of anisotropic materials with tunable anisotropy ratios.

In this work, we prepared anisotropic polyvinyl alcohol (PVA) hydrogels by bidirectional ice templating and tuned the alignment of the lamellar structure by changing the magnitude of the second temperature gradient. Then we characterized the mechanical performance by conducting tensile tests in the directions of the first and second temperature gradients. A wide tunable range of anisotropic ratio (1.6-8.3) between tensile moduli in these two directions was achieved. We further quantitatively analyzed the morphologies of the anisotropic hydrogels, by obtaining histograms for lamellar structure orientations based on the SEM images. With this, we successfully extracted the key parameters that describe the extent of alignment. Finally, a micromechanical model based on Eshelby's solution and Mori-Tanaka's mean-field theory was developed to predict the anisotropic mechanical properties of the ice-templated porous hydrogels (Zhao et al., 1989). The theoretical calculations agree with the experimental results. By revealing the correlation between the oriented microstructure and the anisotropic performance of the material, this model can provide guidance for future microstructure design to achieve specified mechanical properties for more anisotropic hydrogels. In addition to the aligned microporous hydrogels resulting from directional crystallization, this model can also predict the mechanical performances of hybrid hydrogels with interacting micro/nano-fillers (Kim et al., 2015; Liu et al., 2015) and fiber-reinforced hydrogels (Cheng et al., 2020; Zhou et al., 2019).

2. Material and methods

2.1 Materials

PVA power (Mw.89000-98000) and sodium citrate dihydrate were purchased from Sigma Aldrich and used without further purification. Sylgard 184 poly (dimethylsiloxane) (PDMS) was purchased from Dow.

2.2 Experimental method: preparation of anisotropic hydrogel

PVA aqueous solutions of various concentrations (2.5 wt.%, 5 wt.%, and 10 wt.%) were prepared by dissolving PVA powder in deionized water under stirring at 90ºC for 2 hours. PVA solutions were poured into 3D printed polylactic acid (PLA) molds without or with PDMS wedges of various angles (‘0º’ without any wedge, 10º, 20º, 30°, 40°, and 50°) inserted at the bottom of the molds, to provide temperature gradients in both vertical and horizontal directions. The molds were wrapped with a thermally insulating tap and put on a -50°C cold plate. After unidirectionally or bidirectionally freezing for 3 hours, the frozen PVA solutions were taken out of the molds and freeze-dried for 12 hours. The dried PVA foams were soaked in a 1.5M sodium citrate solution to form the hydrogels.

2.3 Morphology characterization:

The samples for morphology characterization were prepared by unidirectionally or bidirectionally freezing PVA solutions, followed by freeze-drying. The morphologies of *x*-*y* cross-sections of these samples were observed by scanning electron microscopy (SEM). The SEM images were then processed using Fast Fourier Transformation (FFT) function in ImageJ to obtain the Fourier transformed images. The alignment of lamellar structure in the SEM images was analyzed using the directionality plugin of ImageJ to obtain direction distribution ($p(\theta)$). Statistical parameters including average direction deviation from *y*-direction and standard deviation of directions were calculated by the following equations:

$$Ave_{\mathrm{Dir}} = \sum p_i \left|\theta_i\right| \tag{1}$$

$$Stdv = \sqrt{\sum p_i \left(\theta_i - Ave_{\mathrm{Dir}}\right)^2} \tag{2}$$

where p_i is the probability of the i^{th} alignment angle and θ_i is the i^{th} alignment angle. Parameters required for theoretical calculations including pore diameters and polymer to void ratios were obtained by converting the SEM images to binary images and conducting particle analysis using ImageJ.

2.4 Measurement of mechanical properties

Mechanical properties of anisotropic PVA hydrogels were measured by uniaxial tensile testing in *x*, *y* (second temperature gradient), and *z* (first temperature gradient) directions by CellScale UniVert. Young's modulus and ultimate tensile strength were obtained from the stress-strain curves. Anisotropic ratios were calculated by:

$$AR = \frac{E_z}{E_y} \tag{3}$$

where E_y and E_z are Young's modulus in *y* and *z* directions, respectively.

Poisson's ratio was measured by taking photos during tensile tests and then calculating the ratio of transverse strain to axial strain.

$$\nu = -\frac{\varepsilon_{\mathrm{width}}}{\varepsilon_{\mathrm{length}}} \tag{4}$$

2.5 Thermal simulation

The time-dependent temperature profiles along the surfaces of wedges of various angles were obtained by using the module of Heat Transfer in Solids and Fluids in COMSOL Multiphysics. The model setup, choice of parameters, and simulation procedure are described in detail in Supporting Information.

3 Experimental results and discussion

3.1 Effect of PVA concentration on pore morphology

3D illustration of the structures produced by unidirectional or bidirectional freezing is shown in Fig. 1. During the ice templating process, the temperature at the surface of the cold plate is lower than the freezing temperature of ice, as well as the temperature of the PVA solution. Thus, a temperature gradient in the vertical direction exists in the solution, which causes the ice crystals to grow upwards. This process is termed 'unidirectional freezing' where there is only a temperature gradient along the vertical direction and the temperature is uniform on the horizontal cold surface. When a PDMS wedge with a certain angle is inserted at the bottom of the mold right on top of the cooling plate, there is still a temperature gradient in the vertical direction. Meanwhile, since the heat will also slowly conduct in the PDMS wedge, there will also be a second temperature gradient along the inclined wedge surface. This process is termed 'bidirectional freezing'. The shape and size of these ice crystals are affected by PVA molecules since they inhibit ice recrystallization by binding to the prism faces of ice crystals (Bachtiger et al., 2021), and this effect is more pronounced with higher PVA concentration (Budke and Koop, 2006). To determine an appropriate PVA concentration for fabricating anisotropic PVA hydrogels with lamellar structures, the effect of PVA concentration on the morphology of pores was first studied. Aqueous solutions of 10 wt.%, 5 wt.%, and 2.5 wt.% PVA was bidirectionally frozen with PDMS wedges of 40^{o}, and the resulting pore sizes and shapes are shown in Fig. S1. For 10 wt.% PVA, the pore diameter is around several microns, while for lower PVA concentrations, the feature sizes increase significantly to 20-50 microns. Although all three samples were prepared with both vertical (1st) and horizontal (2nd) temperature gradients, the 10 wt.% PVA sample has round pores, the 5 wt.% PVA sample shows slight pore elongation, and the 2.5 wt.% PVA sample displays lamellar structure, because the growth of ice crystals along the horizontal temperature gradient was suppressed by the high concentration (10 wt.%) PVA chains, while for less concentrated PVA solutions, ice crystals were able to extend in that direction Since the anisotropy in *x-y* plane is a key feature for the tunability of mechanical properties in y direction, 2.5 wt.% PVA solution was chosen for the fabrication of PVA hydrogels with tunable anisotropy ratios.

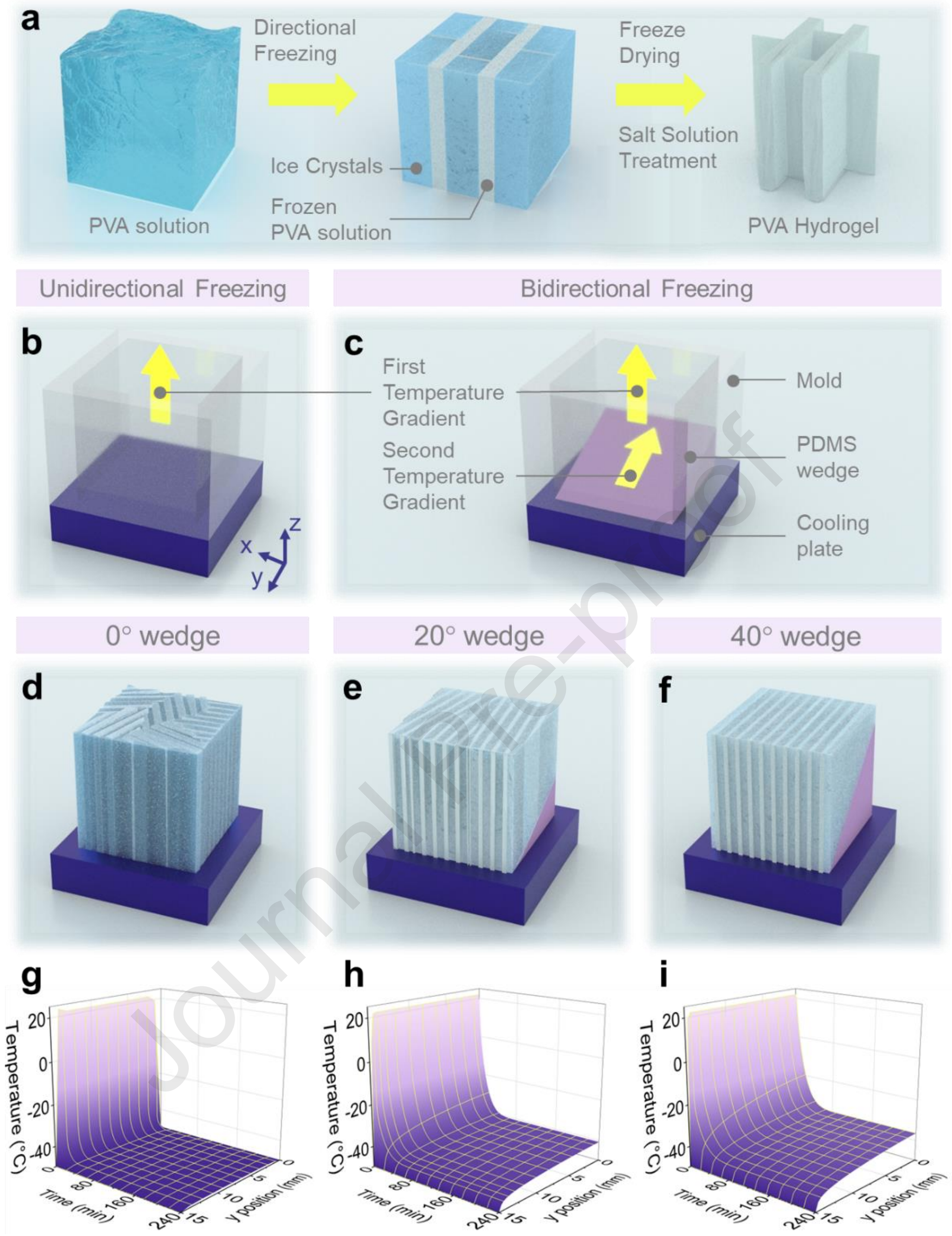

Fig. 1. a) Schematics of the fabrication steps. b) Experiment setup of unidirectional freezing. The direction of the temperature gradient is indicated by the yellow arrow. There is no temperature gradient along the horizontal surface of the cooling plate. c) Experiment setup of bidirectional freezing. The directions of temperature gradients are indicated by the yellow arrows. Apart from the vertical temperature gradient, there is also a temperature gradient along the inclined surface of the PDMS wedge. d)-f) Illustration of the directional freezing experimental setups with d) no wedge, e) a 20° wedge, and f) a 40° wedge. g)-i) Time-dependent temperature profiles along the *y*-direction on the surface of cooling plate simulated using COMSOL Multiphysics, corresponding to d), e) and f), respectively.

3.2 Effect of wedge angle on the alignment of lamellar structure

The temperature gradient in the *z*-direction facilitates the growth of lamellar structure in the vertical direction. However, the normal of the lamellae can take any random orientation in the *x-y* plane. To achieve tunable mechanical properties in the *y*-direction, the normal directions of the planes need to go through a gradual transition from a randomly oriented state to a completely aligned state. Such structures can be fabricated by introducing a second temperature gradient in the *y*-direction (Bai et al., 2015), which is generated by inserting PDMS wedges of various angles at the bottom of the molds. The change of temperature profile on the wedge surfaces with time was obtained by heat transfer simulation using COMSOL Multiphysics. As depicted in Fig. 1d-f, the temperature near the top of the wedges drops more slowly than at the tip of the wedges, and the larger the wedge angle, the slower the temperature change at the top. The calculation of the temperature difference between the top and bottom of the wedges reveals that, for various wedge angles, the temperature differences all dropped rapidly in the first hour, then they reached constant values, which increase with increasing wedge angles (Fig. S2).

The slope of the wedges affects the nucleation and growth of ice crystals, and thus influences the alignment of lamellar structures. During ice templating, ice crystals will nucleate when a certain degree of supercooling is reached, then the crystals will propagate in the directions determined by the local temperature gradient (Bai et al., 2015). In our experiment setup, heat transfer mostly happens through the PDMS wedge and subsequently through the PVA solution, but there is also inevitable heat transfer through the mold walls, causing an additional temperature gradient in the x-direction. At a small wedge angle, heat transfer through the PDMS wedge is faster than through the mold walls, so that ice nucleation mostly happens across the surface of the wedge at an earlier stage of ice templating. Meanwhile, the temperature gradient in the y-direction does not dominate over the temperature gradient in the x-direction, causing the nucleated ice crystals to grow in more random directions. At a large wedge angle, heat transfer across the mold walls becomes more significant compared to through thicker PDMS, resulting in lower temperature on mold walls than on the surface of the PDMS wedge. In this case, ice nucleation will more preferably happen at the edges of the PDMS wedge in contact will the walls rather than all across the PDMS surface. This ununiform nucleation, together with the additional temperature gradient in the x-direction, results in less aligned growth of ice crystals. Consequently, as the wedge angle increases, the alignment of ice crystals will become more ordered until an optimum angle is reached, after which the alignment will become more random. Fig. 2 compares the *x-y* plane morphology via SEM images of hydrogels prepared with different wedge angles, as well as their Fourier transformed images and the directionality histograms. Freezing with 0^{o} wedge angle is essentially unidirectional freezing, which produces many domains of vertical lamellar structure with different orientations. The Fourier transformation of the SEM exhibits circular symmetry, indicating no preferred alignment direction of the structure (Taylor et al., 2013). A more quantitative analysis of the alignment is provided by the directionality histogram, which shows the percentage of domain area of different orientations. In this case, the probabilities of finding the lamella orienting in different directions are similar, indicating that the material is mostly isotropic in the *x*-*y* plane on the macroscopic scale. As the wedge angle increases towards 40º, the temperature gradient in the *y*-direction increases, and the ice crystals have a higher tendency of extending in the *y*-direction besides growing in the *z*-direction, thus the lamellar structures are better aligned. As a result, the sizes of the domains increase while the orientations of the domains approach 0º (*y*-direction, direction of second temperature gradient). On the Fourier transformed images, the gathering of the signal along the vertical lines becomes more prominent, meaning that the structures exhibit increasingly more ordered alignment in the *y*-direction, and the intensity reaches a maximum on the 40º Fourier transformed image, which corresponds to a structure close to perfect alignment. The directionality histograms also show that the orientation of the structures concentrates more at 0º when the wedge angle increases to 40º. On the one hand, these results reveal an optimum wedge angle for lamellae alignment, on the other hand, the gradual change of the degree of alignment indicates the continuous tunability of material performance.

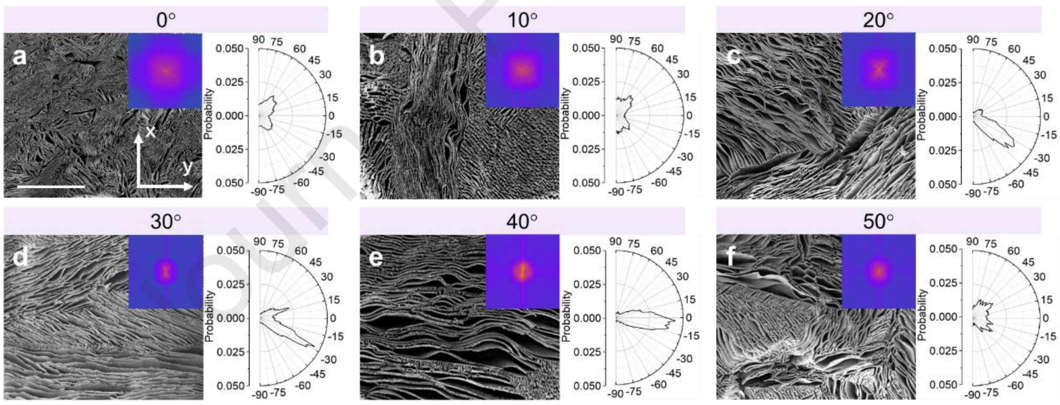

Fig. 2. Orientations of lamellar structures prepared with different wedge angles (a-f, in the order of 0 º, 10 º, 20 º, 30 º, 40 º, and 50 º), shown by the SEM images of *x*-*y* planes, with their corresponding Fourier transformed images (inserts) and directionally histograms (right). Scale bars are 1 mm.

The alignment of the lamellar structures can be further analyzed by calculating the average orientation deviation from the *y*-direction (Fig. 3a) and the standard deviation of the orientation distributions (Fig. 3b). The absolute value of the orientation deviation from the *y*-direction is a measure of the misalignment. Theoretically, for a random distribution of orientations, the average orientation deviation from the *y*-direction should be 45 º, which agrees with the experimental result for 0 º wedge angle. With increasing wedge angle and thus larger temperature gradient in the *y*-direction, lamellae will take less random orientations and align closer to 0 degrees with the *y*-direction. The standard deviation quantifies the width of the distribution. The lowest standard deviation at 40 º wedge angle means that at this fabrication condition, the lamellae grow in a narrower range of orientation than at other wedge angles.

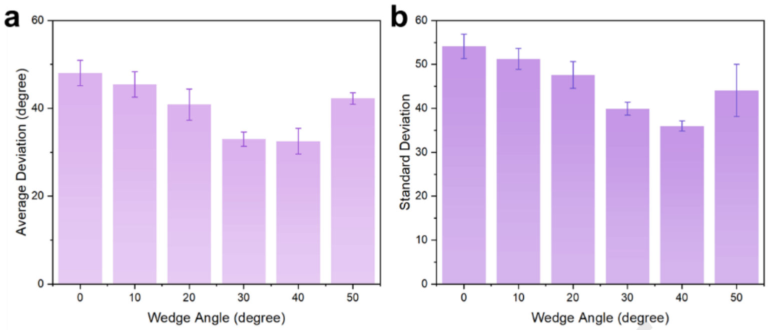

Fig. 3. Directionality analysis of the structure alignment. a) Average of the deviation of alignment directions from y-direction in different domains. b) Standard deviation of alignment direction distribution.

3.3 Mechanical properties

The mechanical performance of the anisotropic PVA hydrogels was characterized by tensile tests in y and z directions. The tensile moduli, ultimate tensile strengths, and representative stress-strain curves in the y or z-direction are shown in Fig. 4. As the wedge angle increases from 0º to 40º, the anisotropic materials become stronger in the y-direction, with 4 times increase in tensile modulus and 5 times increase in ultimate tensile strength, then the properties drop at 50º, while the mechanical properties in the z-direction only change insignificantly. These results corroborate the structure analysis in Fig. 2. The lamellar structures are aligned to a higher extent when the wedge angle increases from 0º to 40º, then becomes less aligned when the angle is further increased to 50º. However, the lamellae are aligned, their normal directions are perpendicular to the z-direction, thus the alignment will not affect the properties in the z-direction. The resulting anisotropy ratio between the moduli in the z and y directions thus varies accordingly between 1.6 and 8.3, which decreases with increasing y-direction modulus. When the wedge angle is further increased to 50º, the mechanical properties drop back down to a similar level as the 30º samples. The trend of mechanical property variation agrees with the trend for lamellar structure alignment revealed in Fig. 3, indicating a correlation between the structural alignment and mechanical performance of the anisotropic material.

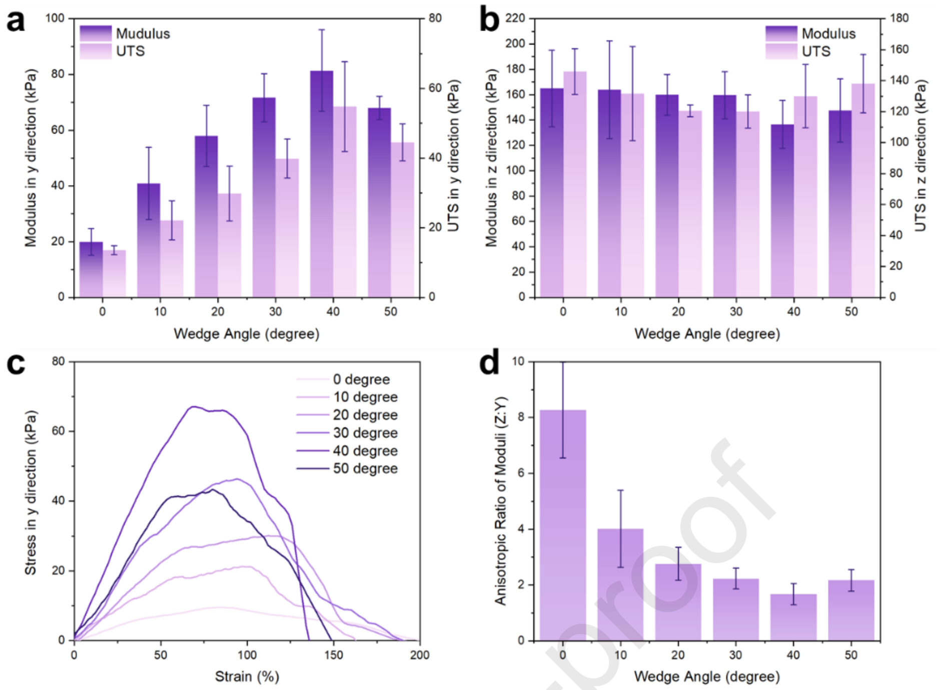

Fig. 4. Tensile properties of anisotropic PVA gels. a) Tensile modulus and ultimate tensile strength (UTS) in the *y*-direction. b) Tensile modulus and ultimate tensile strength (UTS) in the *z*-direction. c) Representative stress-strain curves in the *y*-direction. d) Anisotropic ratio between tensile moduli in *z* and *y* directions.

4. Theoretical prediction of anisotropic ratios

4.1 Modeling of the anisotropic structures

In this section, a micromechanical model was developed to reveal the structure-property correlation of the anisotropic materials. Eshelby's equivalence principle (Eshelby, 2007, 1957) and Mori-Tanaka's mean-field theory (Tanaka and Mori, 1973) were used to correlate the microstructures and mechanical properties of the ice-templated anisotropic hydrogels. The theoretical values of the effective moduli and their anisotropic ratios calculated by this model agree well with the experimental values. In addition to porous hydrogels, this model can also predict the mechanical performances of various anisotropic hydrogel composites with microstructures of different sizes, shapes, and orientations, such as hybrid hydrogels with interacting micro/nano-fillers (Kim et al., 2015; Liu et al., 2015) and fiber-reinforced hydrogels (Cheng et al., 2020; Zhou et al., 2019).

In this study, the important microscopic parameters are porosity, pore shape, and orientation, while the macroscopic properties of interest are the effective elastic moduli and anisotropic ratios of the porous hydrogels. The shape and size of pores are generally represented by the lengths of the three major axes of the ellipsoid a_1, a_2, and a_3, which can be spherical ($a_1 = a_2 = a_3$), oblate ($a_1 < a_2 = a_3$), prolate ($a_1 > a_2 = a_3$), penny shaped ($a_1 << a_2 = a_3$), elliptic cylinder ($a_1 \rightarrow \infty$) and etc. The lamellar structures assembled with the temperature gradients can be abstracted as elliptic cylinders based on the SEM images (Fig. 2). The pore orientation in three-dimensional space can be described by a coordinate transformation matrix with three rotational angles, $\mathbf{R}(\theta, \psi, \gamma)$. Since the global 1-axis and local 1'-axis always coincide for cylindrical inclusions, there exists only one unconstrained rotational degree of freedom in the 2-3 plane. The transformation matrix between the global and local frames is reduced to a matrix containing only one rotational angle θ around the 1(1') axis, as in Eq. (5). The global coordinate system (1-2-3) fixed on the porous material and the local coordinate system (1'-2'-3') attached to the pores are defined in Fig. 5, where axis 1 and axis 3 indicate the direction of the first and second temperature gradients. The pore distribution in the 2-3 plane can be characterized by a probability density function $p(\theta)$. This function can be obtained from the 2-3 plane SEM morphology images and the Fourier transformed images (Fig. 2). This modeling approach is able to evaluate the effective moduli and anisotropic ratios of microporous hydrogels if the aforementioned micromechanical properties are known. The pore interactions at finite concentrations are taken into account (Tandon and Weng, 1987).

$$\mathbf{R}(\theta)=\begin{bmatrix} 1 & 0 & 0 \\ 0 & \cos\theta & \sin\theta \\ 0 & -\sin\theta & \cos\theta \end{bmatrix} \tag{5}$$

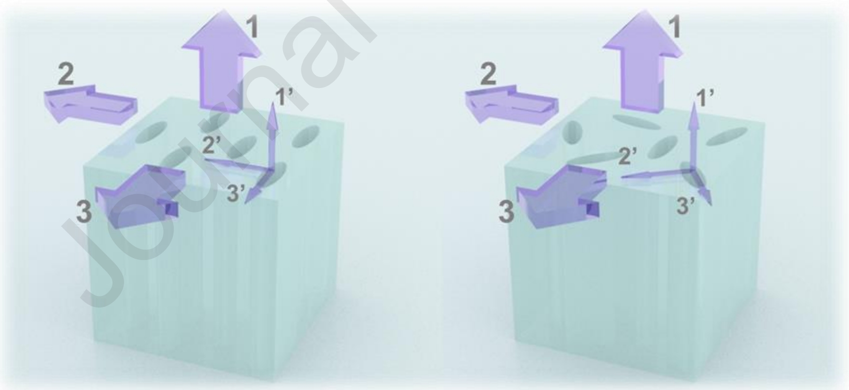

Fig. 5. Illustration of porous material with the global (1-2-3) and local (1'-2'-3') axis.

4.2 Derivation of Eshelby's inclusion problem

Introduce a comparison material with the same shape and elastic properties as the matrix of the composite (porous) material. The matrix is referred to as phase 0, and the inclusions (pores) as phase 1, with the volume fraction 1-c_1 and c_1, respectively. Subject both the comparison material and the composite to the same boundary traction, resulting in stress $\bar{\sigma}_{ij}$ in the comparison material.

$$\bar{\sigma}_{ij} = C^0_{ijkl}\varepsilon^0_{kl} \tag{6}$$

where C^0_{ijkl} is the stiffness tensor of the matrix. Here and hereafter, index notations are applied to tensor calculations. The presence of inclusions (pores) causes the average stress and strain in the composite matrix to differ from the comparison material by $\tilde{\sigma}_{ij}$ and $\tilde{\varepsilon}_{ij}$, respectively.

$$\bar{\sigma}_{ij} + \tilde{\sigma}_{ij} = C^0_{ijkl}\left(\varepsilon^0_{kl} + \tilde{\varepsilon}_{kl}\right) \tag{7}$$

The average stress and strain in the inclusions further differ from the surrounding matrix by σ_{ij}^{pt} and ε_{ij}^{pt}, respectively.

$$\bar{\sigma}_{ij} + \tilde{\sigma}_{ij} + \left\langle \sigma^{pt}_{ij} \right\rangle = C^1_{ijkl}\left(\varepsilon^0_{kl} + \tilde{\varepsilon}_{kl} + \left\langle \varepsilon^{pt}_{kl} \right\rangle\right) = C^0_{ijkl}\left(\varepsilon^0_{kl} + \tilde{\varepsilon}_{kl} + \left\langle \varepsilon^{pt}_{kl} - \varepsilon^*_{kl} \right\rangle\right) \tag{8}$$

where C^1_{ijkl} is the stiffness tensor of the inclusions. ε_{ij}^* is Eshelby's equivalence transformation strain or known as eigenstrain (Mura, 2013). $\langle \cdot \rangle$ denotes the orientational average of the stated quantity with angle θ varying from $-\pi/2$ to $\pi/2$, which is defined as

$$\langle \cdot \rangle = \int_{-\pi/2}^{\pi/2} (\cdot)\, p(\theta)\, d\theta \tag{9}$$

For porous materials, the stiffness C^1_{ijkl} is zero; therefore, Eq. (8) can be further simplified as Eq. (10). This equivalence also holds for local coordinates [Eq. (11)].

$$\varepsilon^0_{ij} + \tilde{\varepsilon}_{ij} + \left\langle \varepsilon^{pt}_{ij} - \varepsilon^*_{ij} \right\rangle = 0 \tag{10}$$

$$\varepsilon^{0\prime}_{ij} + \tilde{\varepsilon}_{ij}{}' + \varepsilon^{pt\prime}_{ij} - \varepsilon^{*\prime}_{ij} = 0 \tag{11}$$

The perturbed strain can be related to the eigenstrain in the local coordinate system (1'-2'-3') by

$$\varepsilon^{pt\prime}_{ij} = S_{ijkl}\varepsilon^{*\prime}_{kl} \tag{12}$$

where S_{ijkl} is the fourth-order Eshelby's tensor. Detailed expressions of S_{ijkl} for elliptic cylindrical inclusions can be found in **Appendix 1** or (Zhao and Weng, 1990). The volume-weighted average of stresses in the inclusions and matrix must be balanced with the overall stress $\bar{\sigma}_{ij}$ and strain $\bar{\varepsilon}_{ij}$ as in Eq. (13) and (14), respectively.

$$\tilde{\sigma}_{ij} = -c_1\left\langle \sigma^{pt}_{ij} \right\rangle \text{ or } \tilde{\varepsilon}_{ij} = -c_1\left\langle \varepsilon^{pt}_{ij} - \varepsilon^*_{ij} \right\rangle \tag{13}$$

$$\bar{\varepsilon}_{ij} = \varepsilon^0_{ij} + c_1\left\langle \varepsilon^*_{ij} \right\rangle \tag{14}$$

The effective elastic tensor is defined as in Eq. (15). The central idea in determining the overall elastic properties C_{ijkl} of the composite is to express the eigenstrain $\left\langle \varepsilon^*_{kl} \right\rangle$ in terms of ε^0_{kl}. All the variables expressed in local coordinates [Eq. (11)]

should eventually be transformed into global coordinates.

$$C_{ijkl}=\frac{\bar{\sigma}_{ij}}{\bar{\varepsilon}_{kl}}=\frac{C^0_{ijkl}\varepsilon^0_{kl}}{\varepsilon^0_{kl}+c_1\left\langle\varepsilon^*_{kl}\right\rangle} \tag{15}$$

4.3 Numerical calculations of anisotropic ratios

Case 1: Aligned pores assembled from dual temperature gradients

When the PDMS wedge angle is 40°, the pores have good alignment under the effect of dual temperature gradients (Fig. 2e), and the material is close to orthotropic. The effective modulus ratio E_{11}/E_{33} for the directions of the two temperature gradients is of our interest. For ideal alignment, the probability density function $p(\theta)$ can be written in the form of Dirac delta function $\delta(\theta = 0°)$. However, in order not to lose generality, we hereby assume that the orientations of the pores are not ideal and use the experimentally measured probability distribution for calculation. Substituting Eq. (12) into Eq. (11) yields the relationship between $\varepsilon^{*\prime}_{ij}$ and $\varepsilon^{0\prime}_{ij}+\tilde{\varepsilon}_{ij}{}'$ given by Eq. (16).

$$\begin{bmatrix}\varepsilon^{*}_{11}{}'\\ \varepsilon^{*}_{22}{}'\\ \varepsilon^{*}_{33}{}'\end{bmatrix}=\frac{1}{A}\begin{bmatrix}A & 0 & 0\\ A_{21} & A_{22} & A_{23}\\ A_{31} & A_{32} & A_{33}\end{bmatrix}\begin{bmatrix}\varepsilon^{0}_{11}{}'+\tilde{\varepsilon}_{11}{}'\\ \varepsilon^{0}_{22}{}'+\tilde{\varepsilon}_{22}{}'\\ \varepsilon^{0}_{33}{}'+\tilde{\varepsilon}_{33}{}'\end{bmatrix} \tag{16}$$

$$\varepsilon^{*}_{12}{}'=\frac{1}{1-S_{1212}}\left(\varepsilon^{0}_{12}{}'+\tilde{\varepsilon}_{12}{}'\right),\ \varepsilon^{*}_{13}{}'=\frac{1}{1-S_{1313}}\left(\varepsilon^{0}_{13}{}'+\tilde{\varepsilon}_{13}{}'\right),\ \varepsilon^{*}_{23}{}'=\frac{1}{1-S_{2323}}\left(\varepsilon^{0}_{23}{}'+\tilde{\varepsilon}_{23}{}'\right)$$

where the expressions of A and A_{ij} are given in **Appendix 2**, $\varepsilon^{0\prime}_{ij}$ and $\tilde{\varepsilon}_{ij}{}'$ can be directly transformed into global coordinates by

$$\varepsilon_{ij}{}'=R_{ik}R_{jl}\varepsilon_{kl} \tag{17}$$

The expression of R_{ij} is given by Eq. (5). The orientation-dependent eigenstrain can be evaluated by taking an orientational average.

$$\left\langle\varepsilon^*_{ij}\right\rangle=\int_{-\pi/2}^{\pi/2}p(\theta)\varepsilon^*_{ij}d\theta=\int_{-\pi/2}^{\pi/2}p(\theta)R_{ki}R_{lj}\varepsilon^{*}_{kl}{}'d\theta \tag{18}$$

Through Eq. (17) and (18), Eq. (16) can be transformed into the global coordinate system, and the relation between $\left\langle\varepsilon^*_{ij}\right\rangle$ and $\varepsilon^0_{ij}+\tilde{\varepsilon}_{ij}$ can be obtained. It is evident that in order to relate $\left\langle\varepsilon^*_{ij}\right\rangle$ and ε^0_{ij} as in Eq. (15), we need to find $\tilde{\varepsilon}_{ij}$. Expanding Eq. (13) yields

$$\tilde{\varepsilon}_{ij}=-c_1\int_{-\pi/2}^{\pi/2}p(\theta)\left(\varepsilon^{pt}_{ij}-\varepsilon^*_{ij}\right)d\theta=-c_1\int_{-\pi/2}^{\pi/2}p(\theta)R_{ki}R_{lj}\left(S_{klmn}-I_{klmn}\right)\varepsilon^{*}_{mn}{}'d\theta \tag{19}$$

where $\varepsilon^{*\prime}_{ij}$ can be expressed in terms of ε^0_{ij} and $\tilde{\varepsilon}_{ij}$ based on Eq. (16) and (17) and I_{ijkl} is the fourth-order identity tensor.

The probability distribution of pores obtained from SEM and Fourier transformed images (Fig. 2) can be fitted with a continuous function. The detailed expressions of the fitting functions $p(\theta)$ for all PDMS wedge angles (0-50°) can be found in Table S2. Different fitting functions should be used for different distribution characteristics, but note that $p(\theta)$ must satisfy the normalization condition.

$$\int_{-\pi/2}^{\pi/2} p(\theta) d\theta = 1 \tag{20}$$

For the lamellar hydrogel with a good alignment, its probability distribution shows a clear Gaussian (normal) distribution $\sum a_i \exp[(b_i-\theta)^2/c_i]$. So far, we have completed all the analytical derivations required to determine the anisotropic ratio of hydrogels between the first and second temperature gradients. Substituting necessary material parameters and probability density functions into the model yields the anisotropic ratio $E_{11}/E_{33} = 1.95$. This theoretical prediction is close to the experimental values $E_{11}/E_{33} = 1.68\pm0.38$.

Case 2: 2D randomly oriented pores and any other orientations
When the PDMS wedge angle is 0°, the pores are randomly oriented in the 2-3 plane (Fig. 2a), and the porous hydrogel is close to transversely isotropic, which indicates that $E_{22} \approx E_{33}$. Ideally, the probability density function can be considered as $1/\pi$. However, without losing generality, a non-ideal $p(\theta)$ can be written as the sum of sine functions $\sum a_i \sin(b_i\theta+c_i)$, where the fitting parameters can be found in Table S2. After substituting the probability density function and material properties into the theoretical model, the anisotropic ratio for longitudinal and transverse moduli is $E_{11}/E_{22} = 7.05$, while the experimental value is $E_{11}/E_{22} = 8.24\pm1.72$. This result successfully verifies the validity of the analytical model and provides theoretical support for the fabrication method of the anisotropic hydrogels.

For any other pore orientations prepared from different PDMS wedge angles (10°, 20°, 30°, and 50°), the detailed probability density functions $p(\theta)$ and the corresponding anisotropic ratios have been summarized in Table S2. In brief, when the wedge angle is 10°, the theoretical $E_{11}/E_{33} = 4.34$, while the experimental value is 3.75±1.39. When the wedge angle is 20°, the theoretical $E_{11}/E_{33} = 2.77$, while the experimental value is 2.76±0.59. When the wedge angle is 30°, the theoretical $E_{11}/E_{33} = 2.41$, while the experimental value is 2.23±0.37. When the wedge angle is 50°, the theoretical $E_{11}/E_{33} = 3.32$, while the experimental value is 2.17±0.39. This theoretical model can effectively predict the anisotropy of all porous hydrogels prepared in this study.

5 Conclusions

In this paper, we prepared PVA hydrogels with tunable anisotropy ratios ranging from 1.68 to 8.27 by bidirectional ice templating. Compared with other fabrication methods, this method provides a wider range of tunability and can be adapted to fabricate a larger volume of anisotropic materials. The thermal simulation shows the increasing trend of temperature difference along the wedges with increasing wedge angle. The morphology analysis reveals that the extent of lamellar structure alignment first increases and then decreases with increasing wedge angle, which exhibits the same trend as mechanical properties in the *y*-direction and anisotropic ratio. To further reveal the determining factor of anisotropic mechanical performance, the apparent elastic moduli at different directions and anisotropy ratios for various wedge angles were calculated using Mori-Tanaka's mean-field theory along with Eshelby's solution. The theoretical calculation effectively relates the lamellar structure alignment with anisotropic mechanical properties, which successfully predicts and provides explanations for anisotropic ratios of various wedge angles. This calculation of the mechanical performance of micro-structured material from bulk properties and structural parameters has the potential of guiding top-down material design.

Acknowledgements

This research was supported by NSF CAREER award 1724526, AFOSR awards FA9550-17-1-0311, FA9550-18-1-0449 and FA9550-20-1-0344, and ONR awards N000141712117 and N00014-18-1-2314.

Declaration of interests

The authors declare no competing interests.

References

Alsaid, Y., Wu, S., Wu, D., Du, Y., Shi, L., Khodambashi, R., Rico, R., Hua, M., Yan, Y., Zhao, Y., Aukes, D., He, X., 2021. Tunable Sponge-Like Hierarchically Porous Hydrogels with Simultaneously Enhanced Diffusivity and Mechanical Properties. Adv. Mater. 2008235. https://doi.org/10.1002/adma.202008235

Bachtiger, F., Congdon, T.R., Stubbs, C., Gibson, M.I., Sosso, G.C., 2021. The atomistic details of the ice recrystallisation inhibition activity of PVA. Nat. Commun. 12. https://doi.org/10.1038/s41467-021-21717-z

Bai, H., Chen, Y., Delattre, B., Tomsia, A.P., Ritchie, R.O., 2015. Bioinspired large-scale aligned porous materials assembled with dual temperature gradients. Sci. Adv. 1. https://doi.org/10.1126/sciadv.1500849

Boley, J.W., Van Rees, W.M., Lissandrello, C., Horenstein, M.N., Truby, R.L., Kotikian, A., Lewis, J.A., Mahadevan, L., 2019. Shape-shifting structured lattices via multimaterial 4D printing. Proc. Natl. Acad. Sci. U. S. A. 116, 20856–20862. https://doi.org/10.1073/pnas.1908806116

Budke, C., Koop, T., 2006. Ice recrystallization inhibition and molecular recognition of ice faces by poly(vinyl alcohol). ChemPhysChem 7, 2601–2606. https://doi.org/10.1002/cphc.200600533

Carnicer-Lombarte, A., Barone, D.G., Dimov, I.B., Hamilton, R.S., Prater, M., Zhao, X., Rutz, A.L., Malliaras, G.G., Lacour, S.P., Bryant, C.E., Fawcett, J.W., Franze, K., 2019. Mechanical matching of implant to host minimises foreign body reaction. bioRxiv. https://doi.org/10.1101/829648

Chai, Q., Jiao, Y., Yu, X., 2017. Hydrogels for biomedical applications: Their characteristics and the mechanisms behind them. Gels 3. https://doi.org/10.3390/gels3010006

Chen, J., Liu, X., Tian, Y., Zhu, W., Yan, C., Shi, Y., Kong, L.B., Qi, H.J., Zhou, K., 2021. 3D-Printed Anisotropic Polymer Materials for Functional Applications. Adv. Mater. https://doi.org/10.1002/adma.202102877

Cheng, J., Jia, Z., Li, T., 2020. A constitutive model of microfiber reinforced anisotropic hydrogels: With applications to wood-based hydrogels. J. Mech. Phys. Solids 138. https://doi.org/10.1016/j.jmps.2020.103893

Courtney, T., Sacks, M.S., Stankus, J., Guan, J., Wagner, W.R., 2006. Design and analysis of tissue engineering scaffolds that mimic soft tissue mechanical anisotropy. Biomaterials 27, 3631–3638. https://doi.org/10.1016/j.biomaterials.2006.02.024

Eiselt, P., Lee, K.Y., Mooney, D.J., 1999. Rigidity of two-component hydrogels prepared from alginate and poly(ethylene glycol)-diamines. Macromolecules 32, 5561–5566. https://doi.org/10.1021/ma990514m

Eshelby, J.D., 2007. The elastic field outside an ellipsoidal inclusion. Collect. Work. J. D. Eshelby 287–295. https://doi.org/10.1007/1-4020-4499-2_25

Eshelby, J.D., 1957. The determination of the elastic field of an ellipsoidal inclusion, and related problems. Proc. R. Soc. London. Ser. A. Math. Phys. Sci. 241, 376–396. https://doi.org/10.1098/rspa.1957.0133

Goh, G.D., Dikshit, V., Nagalingam, A.P., Goh, G.L., Agarwala, S., Sing, S.L., Wei, J., Yeong, W.Y., 2018. Characterization of mechanical properties and fracture mode of additively manufactured carbon fiber and glass fiber reinforced thermoplastics. Mater. Des. 137, 79–89. https://doi.org/10.1016/j.matdes.2017.10.021

Gong, J.P., 2010. Why are double network hydrogels so tough? Soft Matter 6.

Hoffmeister, B.K., Handley, S.M., Wickline, S.A., Miller, J.G., 1996. Ultrasonic determination of the anisotropy of Young's modulus of fixed tendon and fixed myocardium. J. Acoust. Soc. Am. 100, 3933–3940. https://doi.org/10.1121/1.417246

Holzapfel, G.A., Sommer, G., Gasser, C.T., Regitnig, P., 2005. Determination of layer-specific mechanical properties of human coronary arteries with nonatherosclerotic intimal thickening and related constitutive modeling. Am. J. Physiol. - Hear. Circ. Physiol. 289. https://doi.org/10.1152/ajpheart.00934.2004

Hua, M., Wu, S., Ma, Y., Zhao, Y., Chen, Z., Frenkel, I., Strzalka, J., Zhou, H., Zhu, X., He, X., 2021. Strong tough hydrogels via the synergy of freeze-casting and salting out. Nature 590, 594–599. https://doi.org/10.1038/s41586-021-03212-z

Khodambashi, R., Alsaid, Y., Rico, R., Marvi, H., Peet, M.M., Fisher, R.E., Berman, S., He, X., Aukes, D.M., 2021. Heterogeneous Hydrogel Structures with Spatiotemporal Reconfigurability using Addressable and Tunable Voxels. Adv. Mater. 33. https://doi.org/10.1002/adma.202005906

Kim, Y., Yuk, H., Zhao, R., Chester, S.A., Zhao, X., 2018. Printing ferromagnetic domains for untethered fast-transforming soft materials. Nature 558, 274–279. https://doi.org/10.1038/s41586-018-0185-0

Kim, Y.S., Liu, M., Ishida, Y., Ebina, Y., Osada, M., Sasaki, T., Hikima, T., Takata, M., Aida, T., 2015. Thermoresponsive actuation enabled by permittivity switching in an electrostatically anisotropic hydrogel. Nat. Mater. 14, 1002–1007. https://doi.org/10.1038/nmat4363

Lee, Y., Song, W.J., Sun, J.Y., 2020. Hydrogel soft robotics. Mater. Today Phys. 15. https://doi.org/10.1016/j.mtphys.2020.100258

Li, G., Zhang, H., Fortin, D., Xia, H., Zhao, Y., 2015. Poly(vinyl alcohol)-Poly(ethylene glycol) Double-Network Hydrogel: A General Approach to Shape Memory and Self-Healing Functionalities. Langmuir 31, 11709–11716. https://doi.org/10.1021/acs.langmuir.5b03474

Liu, M., Ishida, Y., Ebina, Y., Sasaki, T., Hikima, T., Takata, M., Aida, T., 2015. An anisotropic hydrogel with electrostatic repulsion between cofacially aligned nanosheets. Nature 517, 68–72. https://doi.org/10.1038/nature14060

Ma, Y., Hua, M., Wu, S., Du, Y., Pei, X., Zhu, X., Zhou, F., He, X., 2020. Bioinspired high-power-density strong contractile hydrogel by programmable elastic recoil. Sci. Adv. 6. https://doi.org/10.1126/sciadv.abd2520

McClendon, M.T., Stupp, S.I., 2012. Tubular hydrogels of circumferentially aligned nanofibers to encapsulate and orient vascular cells. Biomaterials 33, 5713–5722. https://doi.org/10.1016/j.biomaterials.2012.04.040

Min, P., Li, X., Liu, P., Liu, J., Jia, X.Q., Li, X.P., Yu, Z.Z., 2021. Rational Design of Soft Yet Elastic Lamellar Graphene Aerogels via Bidirectional Freezing for Ultrasensitive Pressure and Bending Sensors. Adv. Funct. Mater. 31. https://doi.org/10.1002/adfm.202103703

Mura, T., 2013. Micromechanics of Defects in Solids. Springer Sci. Bus. Media. https://doi.org/10.1007/978-94-007-4626-8

Nelson, I., Naleway, S.E., 2019. Intrinsic and extrinsic control of freeze casting. J. Mater. Res. Technol. 8, 2372–2385. https://doi.org/10.1016/j.jmrt.2018.11.011

Nune, S.K., Rama, K.S., Dirisala, V.R., Chavali, M.Y., 2017. Electrospinning of collagen nanofiber scaffolds for tissue repair and regeneration. Nanostructures Nov. Ther. Synth. Charact. Appl. 281–311. https://doi.org/10.1016/B978-0-323-46142-9.00011-6

Roger C. Haut, 2002. Biomechanics of Soft Tissue - Chapter. Handb. Mater. Behav. - Nonlinear Model. Prop. 228–253.

Sadeghi, R., Jahani, F., 2012. Salting-in and salting-out of water-soluble polymers in aqueous salt solutions. J. Phys. Chem. B 116, 5234–5241. https://doi.org/10.1021/jp300665b

Sun, J.-Y., Sun, J.-Y., Zhao, X., Zhao, X., Illeperuma, W.R.K., Illeperuma, W.R.K., Chaudhuri, O., Chaudhuri, O., Oh, K.H., Oh, K.H., Mooney, D.J., Mooney, D.J., Vlassak, J.J., Vlassak, J.J., Suo, Z., Suo, Z., 2012. Highly stretchable and tough hydrogels. Nature 489, 133–136.

Tanaka, K., Mori, T., 1973. Average Stress in Matrix and Average Elastic Energy of Materials With Misfitting Inclusions. Acta Metall. 21, 571–574.

Tandon, G., Weng, G., 1987. Average stress in the matrix and effective moduli of randomly oriented composites. Compos. Sci. Technol. 18, 180.

https://doi.org/10.1016/0010-4361(87)90511-8
Tang, L., Wu, S., Qu, J., Gong, L., Tang, J., 2020. A review of conductive hydrogel used in flexible strain sensor. Materials (Basel). 13. https://doi.org/10.3390/ma13183947
Taylor, S.E., Cao, T., Talauliker, P.M., Lifshitz, J., 2013. Objective morphological quantification of microscopic images using a Fast Fourier Transform (FFT) analysis. Curr. Protoc. Essent. Lab. Tech. 2013. https://doi.org/10.1002/9780470089941.et0905s07
Wang, W., Narain, R., Zeng, H., 2020. Chapter 10 - Hydrogels, in: Polymer Science and Nanotechnology. pp. 203–244.
Wu, J., Zhao, Q., Sun, J., Zhou, Q., 2012. Preparation of poly(ethylene glycol) aligned porous cryogels using a unidirectional freezing technique. Soft Matter 8, 3620–3626. https://doi.org/10.1039/c2sm07411g
Wu, S., Alsaid, Y., Yao, B., Yan, Y., Zhao, Y., Hua, M., Wu, D., Zhu, X., He, X., 2021a. Rapid and scalable fabrication of ultra-stretchable, anti-freezing conductive gels by cononsolvency effect. EcoMat. https://doi.org/10.1002/eom2.12085
Wu, S., Hua, M., Alsaid, Y., Du, Y., Ma, Y., Zhao, Y., Lo, C.Y., Wang, C., Wu, D., Yao, B., Strzalka, J., Zhou, H., Zhu, X., He, X., 2021b. Poly(vinyl alcohol) Hydrogels with Broad-Range Tunable Mechanical Properties via the Hofmeister Effect. Adv. Mater. 33. https://doi.org/10.1002/adma.202007829
Xiao, X., Xiao, X., Zhou, Y., Zhao, X., Chen, G., Liu, Z., Wang, Z., Lu, C., Hu, M., Nashalian, A., Shen, S., Xie, K., Yang, W., Gong, Y., Ding, W., Servati, P., Han, C., Dou, S.X., Li, W., Chen, J., 2021. An ultrathin rechargeable solid-state zinc ion fiber battery for electronic textiles. Sci. Adv. 7. https://doi.org/10.1126/sciadv.abl3742
Yao, B., Scalco de Vasconcelos, L., Cui, Q., Cardenas, A., Yan, Y., Du, Y., Wu, D., Wu, S., Hsiai, T.K., Lu, N., Zhu, X., He, X., 2022. High-stability conducting polymer-based conformal electrodes for bio-/iono-electronics. Mater. Today. https://doi.org/10.1016/j.mattod.2021.12.002
Zhao, Y., Lo, C.Y., Ruan, L., Pi, C.H., Kim, C., Alsaid, Y., Frenkel, I., Rico, R., Tsao, T.C., He, X., 2021. Somatosensory actuator based on stretchable conductive photothermally responsive hydrogel. Sci. Robot. 6. https://doi.org/10.1126/SCIROBOTICS.ABD5483
Zhao, Y., Zhang, B., Yao, B., Qiu, Y., Peng, Z., Zhang, Y., Alsaid, Y., Frenkel, I., Youssef, K., Pei, Q., He, X., 2020. Hierarchically Structured Stretchable Conductive Hydrogels for High-Performance Wearable Strain Sensors and Supercapacitors. Matter 3, 1196–1210. https://doi.org/10.1016/j.matt.2020.08.024
Zhao, Y.H., Tandon, G.P., Weng, G.J., 1989. Elastic moduli for a class of porous materials. Acta Mech. 76, 105–131. https://doi.org/10.1007/BF01175799
Zhao, Y.H., Weng, G.J., 1990. Effective elastic moduli of ribbon-reinforced composites. J. Appl. Mech. Trans. ASME 57, 158–167. https://doi.org/10.1115/1.2888297

Zhou, Y., Hu, J., Liu, Z., 2019. Deformation Behavior of Fiber-Reinforced Hydrogel Structures. Int. J. Struct. Stab. Dyn. 19. https://doi.org/10.1142/S0219455419500329

Appendix 1: Components of Eshelby's tensor S_{ijkl} for elliptic cylinders ($a_1\to\infty$)

$$\begin{aligned}
&S_{1111}=S_{1122}=S_{1133}=0,\quad S_{2211}=\frac{\nu_0}{1-\nu_0}\frac{1}{1+\alpha},\quad S_{3311}=\frac{\nu_0}{1-\nu_0}\frac{\alpha}{1+\alpha}\\
&S_{2222}=\frac{1}{2(1-\nu_0)}\left[\frac{1+2\alpha}{(1+\alpha)^2}+\frac{1-2\nu_0}{1+\alpha}\right],\quad S_{3333}=\frac{\alpha}{2(1-\nu_0)}\left[\frac{\alpha+2}{(1+\alpha)^2}+\frac{1-2\nu_0}{1+\alpha}\right]\\
&S_{2233}=\frac{1}{2(1-\nu_0)}\left[\frac{1}{(1+\alpha)^2}-\frac{1-2\nu_0}{1+\alpha}\right],\quad S_{3322}=\frac{\alpha}{2(1-\nu_0)}\left[\frac{\alpha}{(1+\alpha)^2}-\frac{1-2\nu_0}{1+\alpha}\right]\\
&S_{1212}=\frac{1}{2(1+\alpha)},\quad S_{1313}=\frac{\alpha}{2(1+\alpha)},\quad S_{2323}=\frac{1}{4(1-\nu_0)}\left[\frac{1+\alpha^2}{(1+\alpha)^2}+(1-2\nu_0)\right]
\end{aligned}\tag{21}$$

and other $S_{ijkl}=0$, where $\alpha=a_2/a_3$ is the average aspect ratio of the cross-section of elliptic cylindrical inclusions, and ν_0 is the Poisson's ratio of the composite matrix. Eshelby's tensor possesses the symmetry $S_{ijkl}=S_{jikl}=S_{ijlk}$.

Appendix 2: Expressions of A and A_{ij}

$$\begin{aligned}
&A=S_{2222}S_{3333}-S_{2233}S_{3322}-S_{2222}-S_{3333}+1\\
&A_{21}=S_{2233}S_{3311}+S_{2211}-S_{2211}S_{3333}\\
&A_{22}=1-S_{3333},\quad A_{23}=S_{2233}\\
&A_{31}=S_{2211}S_{3322}-S_{2222}S_{3311}+S_{3311}\\
&A_{32}=S_{3322},\quad A_{33}=1-S_{2222}
\end{aligned}\tag{22}$$

- Achieved wide rage tuning of anisotropic ratio in hydrogel
- Revealed the correlation between microstructure and mechanical performance
- Theoretically predicted anisotropic mechanical property from microstructure

Declaration of interests

☒ The authors declare that they have no known competing financial interests or personal relationships that could have appeared to influence the work reported in this paper.

☐ The authors declare the following financial interests/personal relationships which may be considered as potential competing interests: